INTERNATIONAL JOURNAL FOR NUMERICAL METHODS IN FLUIDS
Int. J. Numer. Meth. Fluids 2010; **62**:660–682
Published online 19 March 2009 in Wiley InterScience (www.interscience.wiley.com). DOI: 10.1002/fld.2036

Numerical modelling of rotating tangential layers (jets) in shells under strong uniform magnetic field

D. K. Fidaros[1], L. Bühler[2], A. P. Grecos[1] and N. S. Vlachos[1,*,†]

[1]*Association Euratom–Hellenic Republic, Department of Mechanical and Industrial Engineering, University of Thessaly, Athens Ave, 38334 Volos, Greece*
[2]*Association FZK-Euratom, Forschungszentrum Karlsruhe, Postfach 3640, D-76021 Karlsruhe, Germany*

SUMMARY

A numerical study of tangential layers in steady-state magnetohydrodynamic rotating flows is presented using CFD to solve the inductionless governing equations. The analysis considers two basic flow configurations. In the first, a fluid is enclosed in a cylinder with electrically perfect conducting walls and the flow is driven by a small rotating, conducting disk. In the second, a flow is considered in a spherical shell with an inner rotating sphere. The fluid in both cases is subjected to an external axial uniform magnetic field. The results show that these flows exhibit two different types of flow cores separated from each other by a tangential layer parallel to the axis of rotation. The inner core follows a solid-body rotation while the outer is quasistagnant. A counter-rotating jet is developed in the tangential layer between the cores. The characteristics of the tangential layer and the properties of the meridional motion are determined for a wide range of Hartmann numbers. Distributions of angular velocity of circumferential flow and electric potential are obtained and the results are compared with those of analytic methods. Copyright © 2009 John Wiley & Sons, Ltd.

Received 16 July 2007; Revised 14 January 2009; Accepted 6 February 2009

KEY WORDS: flow in rotating shells; MHD; tangent layers; counter-rotating jet; CFD

1. INTRODUCTION

Liquid–metal magnetohydrodynamic (MHD) flows are important in various applications and, in particular, in fusion technology. Because of the non-linearity of the governing equations, several

*Correspondence to: N. S. Vlachos, Association Euratom–Hellenic Republic, Department of Mechanical and Industrial Engineering, University of Thessaly, Athens Ave, 38334 Volos, Greece.
†E-mail: vlachos@mie.uth.gr

Contract/grant sponsor: Euratom Fusion Programme and the General Secretariat for Research & Technology (GSRT)
Contract/grant sponsor: Greek Fusion Programme

challenging problems arise and the development of relatively simple but non-trivial models is most useful for a better understanding of the physical processes. Besides their scientific interest, the models considered in this work permit reliable predictions of the flow and the electric field that could be tested experimentally. MHD rotating flows in cylindrical and spherical shells under axial magnetic fields depend strongly on the imposed magnetic field and on the applied kinematic and electrodynamic boundary conditions. They are axisymmetric in nature, known in the relevant literature as $2\frac{1}{2}$D flows, and are of scientific interest to the MHD research community.

In the present work, the effect of a uniform axial magnetic field on the laminar, steady axisymmetric rotating flow of an electrically conducting fluid is investigated. The fluid is enclosed between two coaxial shells (cylindrical or spherical), with the inner rotating and the outer at rest. The walls in contact with the fluid are electric equi-potential surfaces. Irrespective of the magnetic field, the momentum imparted by the rotating disk or sphere (via the viscous action) establishes a pressure distribution in the fluid. The basic objective of the study is to investigate numerically MHD flows in rotating shells using an inductionless approach for low and moderate Hartmann numbers. The main intention is the estimation of the viscous effects in a range of *Ha* numbers, where asymptotic theory no longer applies. Thus, for reasons of brevity and clarity, only necessary numerical details are presented here, and the interested reader is referred to specific published articles or textbooks.

The results show that these flows develop two different types of flow cores, separated from each other by a tangential layer that is parallel to the main axis of rotation. The inner core may be considered to follow a solid-body rotation while the outer is quasistagnant. A counter-rotating jet is developed, which is located in the tangential layer between the cores. The quantitative characteristics of the tangential layer are determined and the properties of the meridional motion are investigated for a wide range of Hartmann numbers. Circumferential and angular velocity fields as well as distributions of the electric potential are obtained and the results are compared with those of analytic methods [1].

Several authors have studied analytically, numerically and experimentally the axisymmetric rotation of a conducting fluid for geometries with different aspect ratios, various orientations of the magnetic field and different values of conductance of the solid boundaries. In the following, only the previous studies directly relevant to the present problem will be discussed.

Antimirov and Molokov [2] employed the method of matched asymptotic expansions to study a steady-state MHD flow driven by a rotating body in a strong, external co-axial magnetic field. The rotating body ejects and absorbs electric current into and from the surrounding fluid and drives, thereby, the rotational motion of the fluid by Lorentz forces. Two major cases were considered; the non-conducting and the super-conducting disk of finite size, where the fluid extends axially and radially to infinity. They specified a map where a 'column' of the conducting liquid rotates at half the angular velocity of the insulating disk. This column rotates at the same angular disk velocity, when it is perfectly conducting. They also defined a region outside of the column where the fluid is at rest, in the first case, and in slight motion in the second. When the fluid is confined in a finite domain, the flow behaves quite differently. Thus, during the rotation of the conducting fluid, a counter-rotating jet is formed at the edge of the rotating disk, as it has been reported by Hollerbach and Skinner [3].

Bessaih *et al.* [4] investigated numerically the flow in a conducting and/or insulated cylindrical cavity with a rotating end-wall under a strong magnetic field. The simulation was performed using the inductionless approach and the results were compared with asymptotic solutions neglecting

DOI: 10.1002/fld

inertial effects. Kharicha *et al.* [5] dealt with the flow driven by one rotating end of a cylindrical cavity filled with a liquid metal. The study was performed for $Re \geqslant 100$ and $0 \leqslant Ha \leqslant 100$ and was focused on thin walls. The aim was to assess the influence of the magnetic field on the corrosion rate caused by the flow of a liquid metal along a metallic wall. One of the conclusions, related to the present study, was that the azimuthal flow is organized into a main core, Hartmann layers and parallel layers. The core flow exhibits a linear variation of circumferential velocity along the axial direction. Bessaih *et al.* [4] and Kharicha *et al.* [5] found a solid-body rotation near the axis. Near the tangent wall the velocity exceeds that of the solid-body rotation and decreases beyond it, in order to satisfy the no-slip condition at the outer wall.

Molokov [6] studied the flow caused by the rotation of an axisymmetric body at constant angular velocity in an external uniform co-axial magnetic field, assuming an infinite flow domain. The fluid follows a solid-body rotation at the same angular velocity only in two extreme cases, when the body is either non-conducting or super-conducting. Molokov also noticed that the perturbations, due to the rotation of a sphere, propagate a large distance along the magnetic field. Dormy *et al.* [7] studied numerically the fluid motion generated in a rotating spherical shell by a slight differential rotation of the inner core in the presence of a magnetic field. Their work suggested the need of a numerical algorithm to solve the thin boundary layers without over-increasing the number of grid points. Starchenko [8] gave an analytic solution for the problem of almost-rigid body rotation of viscous, conducting, spherical layers of a liquid in an axisymmetric magnetic field. Among others, he formulated a description of the shear MHD layers that smoothed out the large gradients at the boundaries of the MHD structures.

Hollerbach and Skinner [3] investigated numerically the flow of an electrically conducting fluid in a spherical shell, with the inner sphere rotating and with a strong magnetic field imposed parallel to the axis of rotation. They noticed the existence of a strong, counter-rotating jet. One of their main conclusions was that, depending on the boundary conditions, the basic state consists of either a shear layer or a counter-rotating jet, both located near the rotating body and becoming thinner and faster, respectively, with increasing magnetic field.

Bühler [1] examined the cases of concentric annular MHD flows using asymptotic methods and showed two different types of cores, which are separated from each other by a tangent shear layer. The inner core performs solid-body rotation while the outer remains entirely stagnant. The fluid near the moving body follows mainly its rotation. The angular velocity of the rotating core decays along the magnetic field lines and vanishes at the non-moving outer wall. The two cores are separated from each other by a viscous layer, tangential to the rotating cylinder where the fluid rotates at high speed in the opposite sense. With increasing magnetic field, the layer becomes thinner and the velocity increases. This fluid behaviour may be due to the difference in the electric potential between the edges of the inner (rotating) and the outer (stationary) fluid core.

Although electrically driven MHD flows are not presently considered, the work of Hunt and Malcolm [9] is mentioned here, who studied experimentally and described analytically a series of such flows. They placed two non-rotating disks on the top and bottom of an insulating container of mercury to which they applied an electric potential difference. They noticed the existence of a thin layer, which is very similar to that of the present work. They also found that a thin layer was created which joined the two disks. In its interior, a large radial electric field and a high circumferential velocity were induced, which increased as the magnetic field became stronger.

DOI: 10.1002/fld

2. MATHEMATICAL FORMULATION

2.1. Governing equations

The governing equations for the steady state, inductionless magnetohydrodynamic flow of an incompressible viscous fluid may be written in dimensionless form as follows:

Momentum conservation:

$$(\mathbf{v}\cdot\nabla)\mathbf{v}=-N\nabla p+\frac{1}{Re}\nabla^2\mathbf{v}+N(\mathbf{j}\times\mathbf{B}) \tag{1}$$

Ohm's law-for moving conducting fluids:

$$\mathbf{j}=-\nabla\varphi+\mathbf{v}\times\mathbf{B} \tag{2}$$

Fluid mass, electric charge conservation:

$$\nabla\cdot\mathbf{v}=0,\quad \nabla\cdot\mathbf{j}=0 \tag{3}$$

In the above equations, $\mathbf{v}$ and $\mathbf{j}$ are the dimensionless velocity and current density vectors, respectively, $\mathbf{B}$ is the externally applied uniform magnetic induction (the induced field being neglected in the presently adopted low-Rm approximation), and p and φ are the pressure and electric potential, all scaled by their reference quantities: u_0, $j_0=\sigma u_0 B_0$, B_0, $\sigma u_0 B_0^2 L$ and $u_0 B_0 L$, respectively. This scaling, in particular, the reference quantity for the pressure is convenient for strong magnetic fields and it has been used to derive asymptotic solutions of the governing equations [1].

The characteristic velocity u_0 is the azimuthal velocity of the rotating body at the symmetry plane and the characteristic length L is the radius of the rotating body. B_0 is the magnitude of the externally applied magnetic induction. The fluid density ρ, electric conductivity σ, and kinematic viscosity v are assumed to be constant. The flow is controlled by two dimensionless parameters, namely the Hartmann number, Ha, (or interaction parameter, N) and the Reynolds number, Re, defined as:

$$Ha=B_0 L\sqrt{\frac{\sigma}{\rho v}} \tag{4}$$

$$N=\frac{\sigma L B_0^2}{\rho u_0}=\frac{Ha^2}{Re} \tag{5}$$

$$Re=\frac{u_o L}{v} \tag{6}$$

It should be noted that the square of the Hartmann number represents the ratio of the electromagnetic to viscous forces while the interaction parameter indicates the ratio of the electromagnetic to inertia forces. From Equation (2), assuming that the magnetic induction is parallel to the axis of rotation ($\mathbf{B}=\mathbf{z}_0$, where $\mathbf{z}_0$ the unit vector in the z-direction) and taking into account that the flow is axisymmetric, the three components of Equation (1) in cylindrical coordinates read

$$\frac{Re}{Ha^2}(V_r\partial_r V_r+V_z\partial_z V_r-\omega^2 r)=-\partial_r p+\frac{1}{Ha^2}\left(\Delta V_r-\frac{V_r}{r^2}\right)-V_r \tag{7}$$

$$\frac{Re}{Ha^2}\left(V_r\partial_r\omega+V_z\partial_z\omega+\frac{2}{r}\omega V_r\right)=\frac{1}{Ha^2}\left(\Delta\omega+\frac{2}{r}\partial_r\omega\right)+\frac{1}{r}\partial_r\varphi-\omega \tag{8}$$

DOI: 10.1002/fld

$$\frac{Re}{Ha^2}(V_r\partial_r V_z + V_z\partial_z V_z) = -\partial_z p + \frac{1}{Ha^2}(\Delta V_z) \tag{9}$$

where V_r, V_z are the radial and axial velocities, respectively, $V_\theta = \omega \cdot r$ is the circumferential velocity, and ω is the angular velocity of the fluid. In addition, for the present axisymmetric flows, the Laplacian operator for a variable f is given in cylindrical coordinates by: $\Delta f = \partial^2_{rr} f + \frac{1}{r}\partial_r f + \partial^2_{zz} f$.

From Equations (2) and (3) it follows that

$$\Delta\varphi = 2\omega + r\partial_r\omega \tag{10}$$

Equation (10) is solved numerically in the same manner as the transport Equations (7)–(9).

Finally, the mass continuity for the present incompressible fluid must be added:

$$\frac{1}{r}\partial_r(rV_r) + \partial_z V_z = 0 \tag{11}$$

2.2. *Boundary conditions*

The geometry of the rotating disk in the cylindrical container (case A) and the coordinate system are shown in Figure 1(a). The liquid metal fills a cylinder of radius $R=3$ and height $Z=3$ and it is submitted to an axial magnetic field $\mathbf{B}=\mathbf{z_0}$. The upper and the vertical (right) boundaries form the perfectly conducting walls of the cylindrical shell. The left boundary is the symmetry axis while the conducting zero-thickness rotating disk is placed at the bottom ($0<r<1$). A symmetry condition is applied to the rest of the lower boundary ($1<r<R$).

The geometry and the coordinate system of the two concentric perfectly conducting spheres (case B) are presented in Figure 1(b). An inner sphere rotating at constant speed is driving the conducting fluid flow while the outer sphere is stationary. The radius of the inner sphere is $r=r_0=1$ and of the outer $r=R=3$. Moreover, symmetry is assumed with respect to the plane $z=0$.

Closure of the electric currents depends strongly on the electric properties of the walls and consequently, the Lorentz force and the velocity field are governed by these properties. In general,

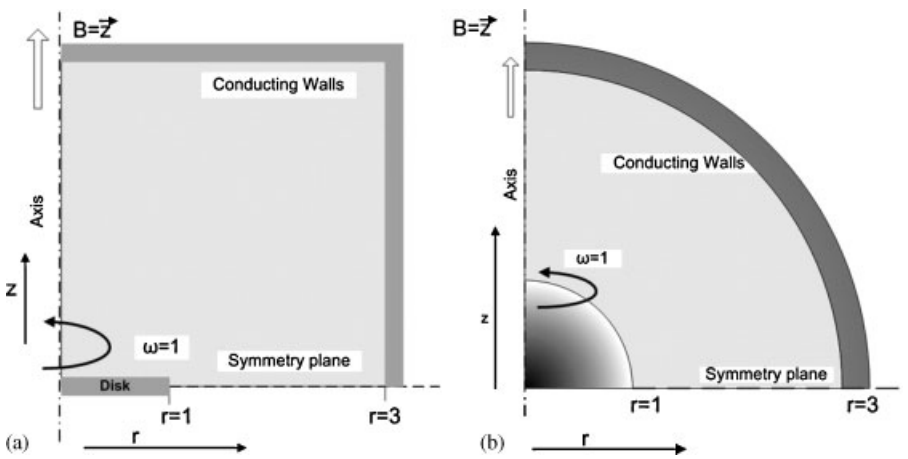

Figure 1. Geometry and boundary conditions for the rotating disk in a cylinder (a) and for the sphere rotating in a spherical shell (b).

DOI: 10.1002/fld

the electromagnetic boundary conditions depend mainly on the ratio of wall-to-fluid conductivity, and on the ratio of wall thickness to the fluid depth [10]. In the present study, where the walls are assumed perfect electric conductors, we may take that $\varphi=0$ at the outer walls. The electric potential at the rotating body is a known function $\varphi(r)$ of radius as described below. At all solid boundaries a no-slip condition is assumed, implying that at the outer walls the velocity vanishes, while the fluid moves with the same speed at the rotating body.

The boundary and symmetry conditions for the velocity and electric potential are

$$\partial_r\omega=0, \quad \partial_r V_z=0, \quad V_r=0, \quad \partial_r\varphi=0 \quad \text{for } r=0, 0<z<Z \tag{12}$$

$$\omega=1, \quad V_z=0, \quad V_\mathrm{r}=0, \quad \varphi=\varphi_\mathrm{b}(r) \quad \text{for } z=0, 0<r<1 \tag{13}$$

$$\partial_z\omega=0, \quad V_z=0, \quad \partial_z V_\mathrm{r}=0, \quad \partial_z\varphi=0 \quad \text{for } z_\mathrm{b}=0 \text{ and } 1<r<R \tag{14}$$

$$\omega=0, \quad V_z=0, \quad V_\mathrm{r}=0, \quad \varphi=0 \quad \text{for } r=R, 0<z<Z \tag{15}$$

where z_b denotes the contour of the rotating body ($z_\mathrm{b}=0$ for the disk, $z_\mathrm{b}=\sqrt{1-r^2}$ for the sphere).

For a perfectly conducting body, the current density is negligible in comparison with the potential gradient and the induced electric field. For rotation at constant angular velocity of circumferential flow $\omega=1$, and $\mathbf{B}=\mathbf{z}_0$, this implies that

$$\nabla\varphi_\mathrm{b}=\mathbf{v}\times\mathbf{B}\Rightarrow\nabla\varphi_\mathrm{b}=V_\theta\mathbf{r}=(\omega\cdot r)\mathbf{r} \tag{16}$$

and finally

$$\partial_r\varphi|_\mathrm{b}=r \tag{17}$$

The electric potential for the rotating body, Figure 2, is obtained by integration:

$$\varphi_\mathrm{b}=\int_0^1(\partial_r\varphi|_\mathrm{b})\,\mathrm{d}r=\frac{1}{2}r^2+C \tag{18}$$

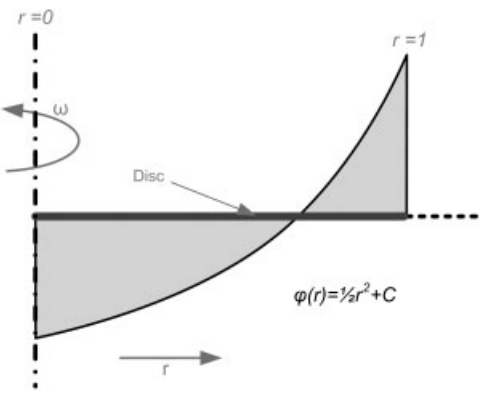

Figure 2. Boundary condition of the electric potential over the rotating disk.

DOI: 10.1002/fld

The integration constant C is determined in such a way that the currents entering the body are balanced by those leaving it. This gives for the rotating disk (case A) the condition that

$$\int_{r=0}^{r=1} (\partial_z \varphi|_b) 2\pi r \, dr = 0 \quad \text{at } z = 0 \tag{19}$$

For the rotating sphere (case B), the integral current upon the spherical surface should vanish. From Equation (2) the wall-normal current becomes

$$j_n = (-\nabla\varphi + \mathbf{v} \times \mathbf{B}) \cdot \mathbf{n} \tag{20}$$

and the global balance of charge at the rotating sphere is

$$\int_s j_n 2\pi r \, ds = \int_s (-\partial_n \varphi) 2\pi r \, ds + \int_s \omega r (\mathbf{r} \cdot \mathbf{n}) 2\pi r \, ds = 0 \tag{21}$$

where s denotes the length along the body contour.

As the radial potential gradient is cancelled by the second term of the right-hand part of Equation (21), it follows:

$$I = \int_s j_n 2\pi r \, ds = \int_0^1 j_z 2\pi r \, dr = \int_0^1 (-\partial_z \varphi|_b) 2\pi r \, dr = 0 \quad \text{at } z = \sqrt{1 - r^2} \tag{22}$$

The values of C in Equation (18) for the two rotating bodies (cases A and B) are obtained using an implicit iterative procedure in such a way that the integral constraints (19) and (22) are satisfied by calculating: $C_i' = -\sum (\partial_z \varphi|_b)_r^i r \, dr_r \ \forall r \in [0, 1] \wedge z_b = 0$, for the disk and $\forall r \in [0, 1] \wedge z_b = \sqrt{1 - r^2}$, for the sphere, while under-relaxation is used to achieve convergence with relative errors smaller than 1.0E–05.

3. NUMERICAL DETAILS

To carry out the numerical simulations, the CFD code CAFFA [11] was extended to a solver suitable for MHD flows. The original version of the code was made available in the Internet (ftp://ftp.springer.de/pub/technik/peric/). This code solves the Navier–Stokes equations for 2D incompressible flows, using finite volumes and structured, collocated curvilinear grids. The code has been recently modified to include more complex discretization schemes by Baxevanou and Vlachos [12]. Furthermore, Fidaros [13] extended the code to account for the Lorentz force appearing in MHD flows, incorporating also faster algorithms for the solution of the resulting linear systems. The Lorentz force is calculated implicitly according to the method described by Cho [14] for inductionless applications. The modified code is now capable to solve both MHD inductionless and full induction problems for incompressible flows, calculating the electric potential and the components of the magnetic induction, respectively. To limit the long execution times, fast Krylov space algorithms for the solution of linear systems have been incorporated.

Equations (7)–(11) have been solved using a finite volume method coupled to a pressure correction based on the SIMPLEC algorithm (see Van Doormaal and Raithby [15], Versteeg and Malalasekera [16]) as described by Ferziger and Peric [11] on a non-uniform collocated grid. It should be noted that all SIMPLE-like solution algorithms obtain the pressure field, via the so-called

DOI: 10.1002/fld

pressure correction equation. This ensures mass conservation via Equation (11), at each computational cell, by updating the velocities obtained from the momentum equations and the pressure field of the previous iteration. The SIMPLE algorithm uses an iterative procedure to calculate the pressure and velocity fields. Starting from initial guessed values, its principal steps are as follows:

(a) Solve the discretized momentum equations to yield intermediate velocities (V_{r}^*, V_z^*).

$$a_p V_{\mathrm{r},p}^* = \sum a_{nb} V_{\mathrm{r},nb}^* - \frac{\delta p^*}{\delta r}\Delta V + S_{V_{\mathrm{r}}}\Delta V \quad \text{and} \quad a_p V_{z,p}^* = \sum a_{nb} V_{z,nb}^* - \frac{\delta p^*}{\delta y}\Delta V + S_{V_z}\Delta V \tag{23}$$

(b) Satisfy local mass continuity in the form of an equation for pressure-correction, p'

$$a_p p'_p = \sum a_{nb} p'_{nb} + S_{p'}\Delta V \tag{24}$$

(c) Correct pressure and velocities:

$$p_p = p'_p + p_p^* \tag{25}$$

$$V_{\mathrm{r},p} = V_{\mathrm{r},p}^* + \frac{1}{a_p}\delta p'\delta z \tag{26}$$

$$V_{z,p} = V_{z,p}^* + \frac{1}{a_p}\delta p'\delta r \tag{27}$$

(d) Solve the discretized transport equations for each scalar property, φ.

$$a_p \varphi_p = \sum a_{nb}\varphi_{nb} + S_\varphi \Delta V_\varphi \tag{28}$$

(e) Use the new values and repeat steps (a)–(d) until the p, V_{r}, V_z and φ fields are all converged.

All the scalar quantities φ are solved implicitly using under-relaxation to ensure solution stability. Following the steps required by the SIMPLE algorithm, the quantities V_{r}, ω, V_z and φ are calculated implicitly from Equations (7)–(10), respectively. All properties and terms in the transport equations are calculated implicitly and consequently the terms of the centrifugal and Lorentz forces.

The solution was obtained in the meridional plane (r–z) by solving Equations (7), (9) and (11) for V_{r}, V_z and p, respectively. These values were then used to obtain ω from Equation (8). The electric potential φ was subsequently computed from Equation (10) using the values of ω in the meridional plane. The spatial, advection and diffusion terms in every equation are discretized with a second-order central difference scheme. The central difference scheme is a second-order numerical scheme providing significantly less numerical (artificial) diffusion, which is essential to this kind of computations. The BiCGSTAB of Krylov space solver predefined by the MSI algorithm [17, 18] was adopted for the numerical solution of the linear set of algebraic equations.

The convergence criterion for all equations solved was set to 1.0E−06, while a typical execution required about 6 h of CPU time on a personal computer with a 4 GHz CPU and 512 MB RAM. These long execution times were due to the slow convergence of the electric potential equation, since the continuously changing boundary values over the rotating body imposed very low relaxation factors, necessary to avoid undesirable numerical oscillations of the velocity field.

The non-uniform grids used for the two geometries are depicted in Figure 3. The proper refinement of the grid is of great importance in order to calculate accurately the very high gradients of velocity and electric potential. The grid for case A (rotating disk in cylindrical shell) consists

DOI: 10.1002/fld

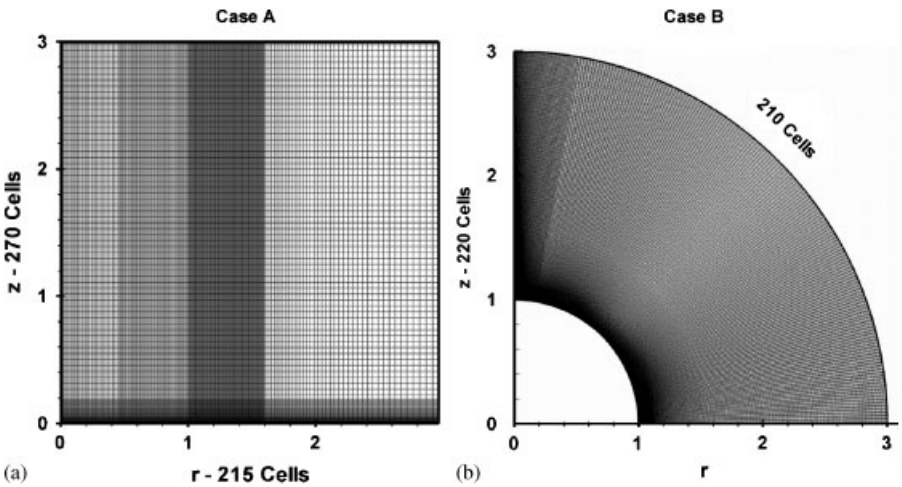

Figure 3. Computational grids for the disk (a) and for the sphere (b).

of 215×270 structured cells and it is finer in two major areas, near the axis and the edge of the rotating disk ($r = 1$) because the high gradients of the angular velocity of the circumferential flow and of the potential in these regions must be resolved properly. For case B (spherical shells), the grid was composed of 210 cells in the outer curvilinear direction and 220 in the radial and it was also finer in two major areas, near the axis and right above the rotating body.

Before the final calculations, the model was successfully validated against the results of Bessaih *et al.* [4] and Kharicha *et al.* [5] for low and moderate *Ha* numbers, and those of Hunt and Malcolm [9] for high *Ha* numbers. In particular, the MHD flow driven by an applied voltage between two circular fixed disk electrodes placed coaxially at two insulating Hartmann walls was studied by Hunt and Malcolm [9]. They noticed the formation of an inner and an outer stagnant core when a voltage was applied between the circular electrodes in mercury at rest. A shear layer developed between the two cores, similar to the present jets, with increasing velocity and decreasing thickness, as the magnetic field was increased. Thus, simulations were performed in order to reproduce the jet formation of the above experiment, using a non-uniform collocated structured mesh with 250×250 cells. Figure 4 shows a comparison of the predicted (filled circles) maximum circumferential velocity of the shear layer with the results of an asymptotic analysis by Bühler [1] of the above experiment (continuous line). The agreement between the numerical and the analytic results is excellent.

In addition, grid independence tests were carried out before the final simulations. Table I shows the results of a grid independence test for the case of the spherical shell using two *Ha* values (200, 300), two convergence criteria (1.0E−05, 1.0E−06) and four different grid sizes ($130 \times 140, 160 \times 170, 190 \times 200, 210 \times 220$). The differences in the predicted magnitude of the maximum angular velocity of the counter-rotating jet and the analytic solution of Bühler [1] are 10% for the coarser grid and less than 0.5% for the finer mesh and the higher convergence criterion.

Finally, it should be noted that the numerical methods used here are fairly standard as the emphasis of the present work was in the MHD aspects of the numerical model. However, there

DOI: 10.1002/fld

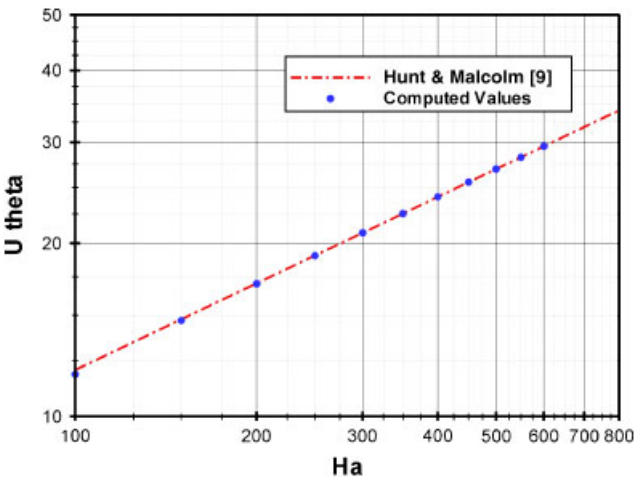

Figure 4. Comparison of the predicted maximum circumferential velocity of the shear layer with that of the asymptotic analysis by Bühler [1] of the experiment of Hunt and Malcolm [9].

Table I. Grid independence test for the spherical shell case.

	Grid size				
Ha	130×140	160×170	190×200	210×220	Analytic Bühler [1]
Convergence criterion $e=1.0\text{E}-06$					
200	1.5372	1.6180	1.7014	1.7232	1.7235
300	1.9471	2.0637	2.1712	2.1944	2.1949
Convergence criterion $e=1.0\text{E}-05$					
200	1.5265	1.6085	1.6739	1.7202	1.7235
300	1.9258	2.0518	2.1266	2.1897	2.1949

are a number of modern numerical methods for incompressible flows, as described by Drikakis and Rider [18] while an interesting work on MHD flow modelling is that of Ni *et al.* [19].

4. RESULTS AND DISCUSSION

4.1. Hydrodynamic case ($Ha=0$)

For the hydrodynamic case, Equations (7)–(9) and (11) were solved for $Ha\to0$, i.e. for a vanishing magnetic field. Note that for this case, Equation (1) reduces to the hydrodynamic Navier–Stokes equation, where the quantity $(Ha^2/Re)\,p$, representing pressure in usual hydrodynamic units, ρu_0^2, remains finite.

Results of angular velocity of circumferential flow and streamlines of the meridional motion (driven by centrifugal forces) for $Re=1$ are shown in Figures 5 and 6 for the rotating disk and

DOI: 10.1002/fld

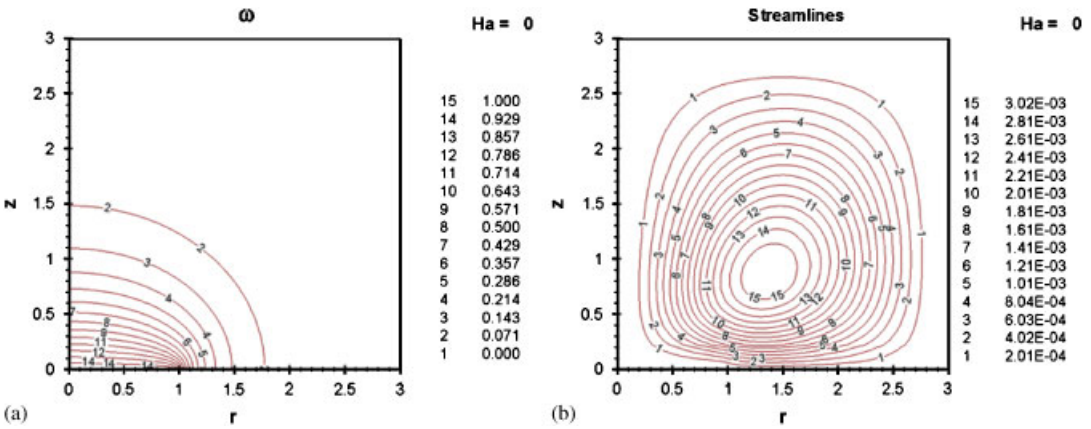

Figure 5. Hydrodynamic flow above a rotating disk (case A) for $Re=1$, $Ha=0$: angular velocity of circumferential flow (a) and streamlines (b) of meridional motion.

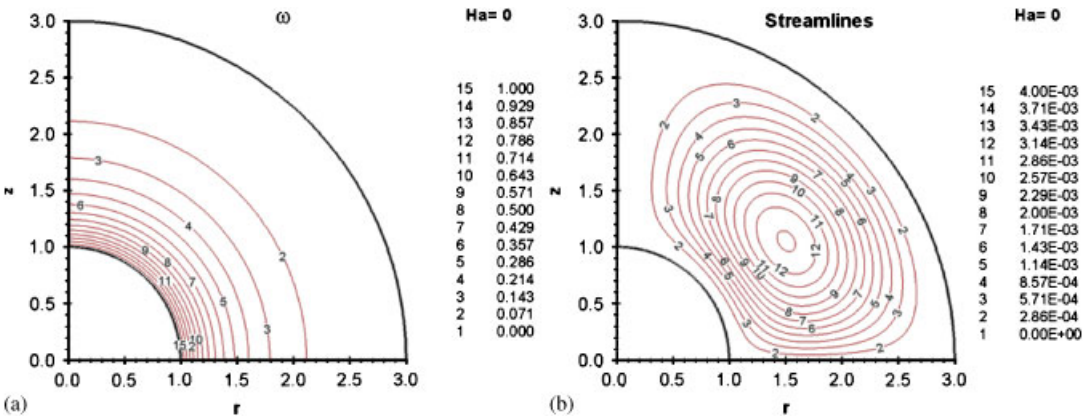

Figure 6. Hydrodynamic flow above a rotating sphere (case B) for $Re=1$, $Ha=0$: angular velocity of circumferential flow (a) and streamlines (b) of meridional motion.

the sphere, respectively. The body rotation causes a revolution of the fluid, which at some distance from the body is driven by viscous shear and exchange of momentum due to the meridional motion. The angular fluid velocity decays from the value of $\omega=1$ at the rotating body to $\omega=0$ at the outer shell. The angular velocity of circumferential flow ω of the fluid just above the rotating body is higher than everywhere in the cavity and decays along the z-direction. The reduction of ω is more intense in the radial than in the axial direction.

4.2. Magnetohydrodynamic case ($Ha>0$)

When the magnetic field is imposed, the behaviour of the fluid is modified. For small Hartmann numbers ($Ha<10$) the changes in the flow are minor, but noticeable. The flow pattern starts

DOI: 10.1002/fld

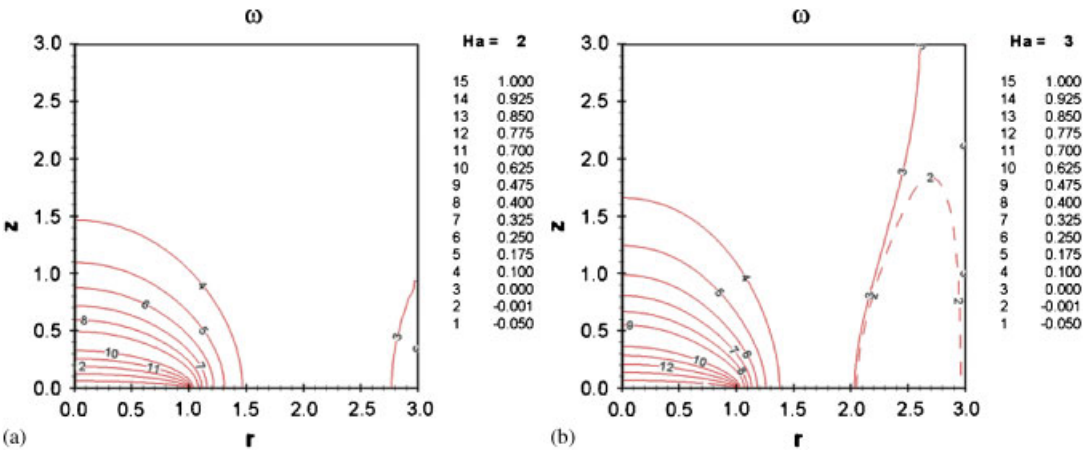

Figure 7. MHD flow above a rotating disk (case A) for $Re=1$. A weak reverse angular velocity appears at $Ha=3$ (right), not observed at $Ha=2$ (left).

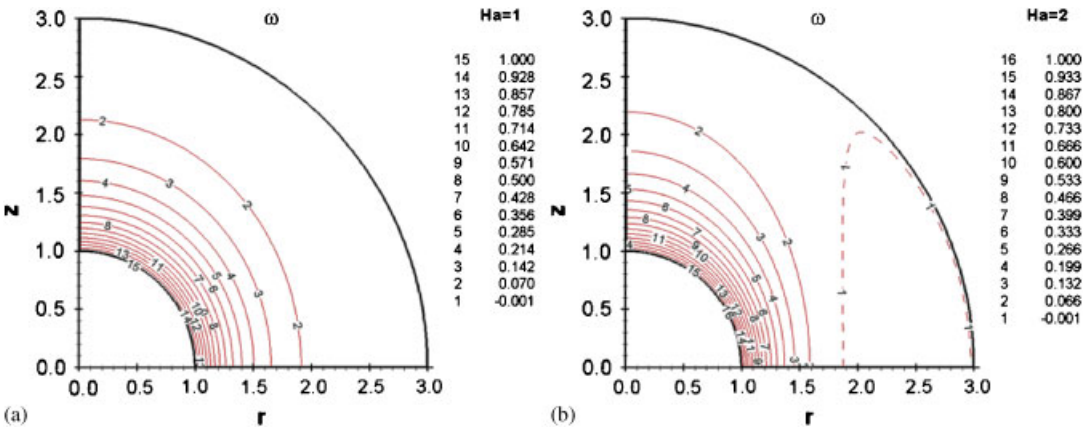

Figure 8. MHD flow above a rotating sphere (case B) for $Re=1$. A weak reverse angular velocity appears at $Ha=2$ (right), not observed at $Ha=1$ (left).

stretching along the axial direction and contracting in the radial in such a way that it is mainly confined to the interior of the so-called tangent cylinder at $r=1$ that forms at the edge of the rotating body along magnetic field lines. Outside the tangent cylinder the flow starts rotating in the reverse direction at Ha between 2 and 3 for the disk (case A) and between $Ha=1$ and 2 for the sphere (case B) as shown in Figures 7 and 8, respectively. For strong magnetic fields ($Ha>10$) two cores are observed inside and outside the tangent cylinder. The rotation of the inner core decays linearly along the magnetic field lines from $\omega=1$ at the disk or sphere to $\omega=0$ at the external wall, while the outer core is practically stagnant. The viscous tangent layer in which a strong reverse flow appears, matches smoothly the velocity difference in the two cores at $r=1$. The intensity of this reversed flow increases with increasing Ha while the layer thickness decreases. Results of the

DOI: 10.1002/fld

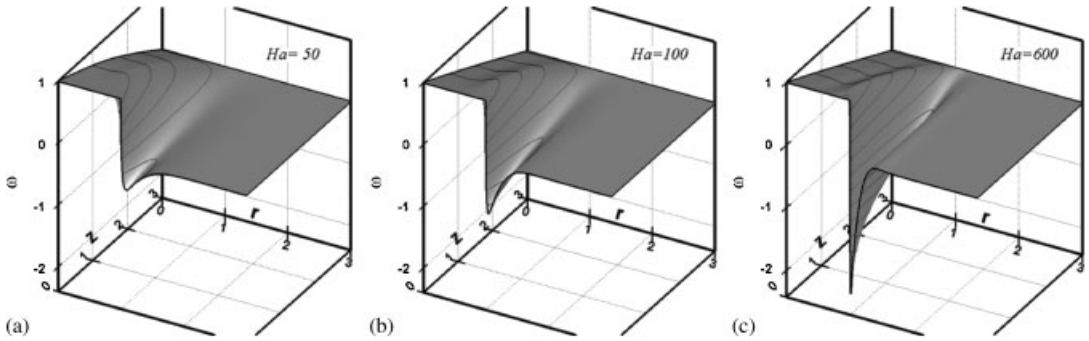

Figure 9. Distribution of angular velocity of circumferential flow $\omega(r, z)$ for a rotating disk (case A). Formation of counter-rotating jet with increasing *Ha*.

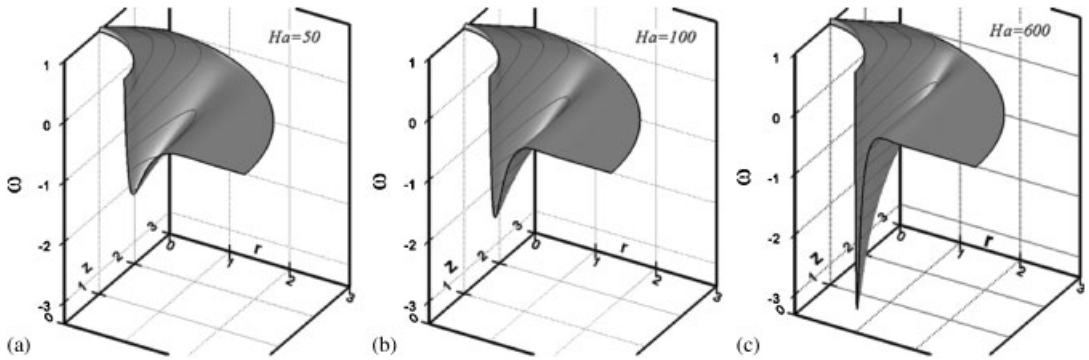

Figure 10. Angular velocity of circumferential flow $\omega(r, z)$ for a rotating sphere (case B). Formation of counter-rotating jet with increasing *Ha*.

angular velocity of circumferential flow are shown for the rotating disk in Figure 9 and for the rotating sphere in Figure 10. It seems worth noting that, for the case of the rotating disk, there are not viscous Hartmann layers forming at the disk and at the outer wall. The core solution here satisfies already the kinematic and electric boundary conditions.

For the case of the rotating sphere, Figure 10, a similar behaviour is observed. There exists an inner core rotating in the sense of the body, a stagnant outer core and a counter-rotating viscous layer that connects smoothly the solutions in both these cores. The electric potential in the core seems to satisfy again the boundary condition at the inner sphere so that for this quantity the viscous Hartmann layers are also unimportant. For the angular velocity of circumferential flow, however, the situation is different. The fluid core above the sphere rotates faster than the sphere itself close to the axis and slightly slower for $r > 0.5$. As a result there appears now a viscous Hartmann layer (see Figure 11) that matches the core solution with the no-slip boundary condition at the surface of the body. This type of behaviour has been already predicted by the asymptotic method of Bühler [1] and by the numerical simulations of Hollerbach and Skinner [3].

DOI: 10.1002/fld

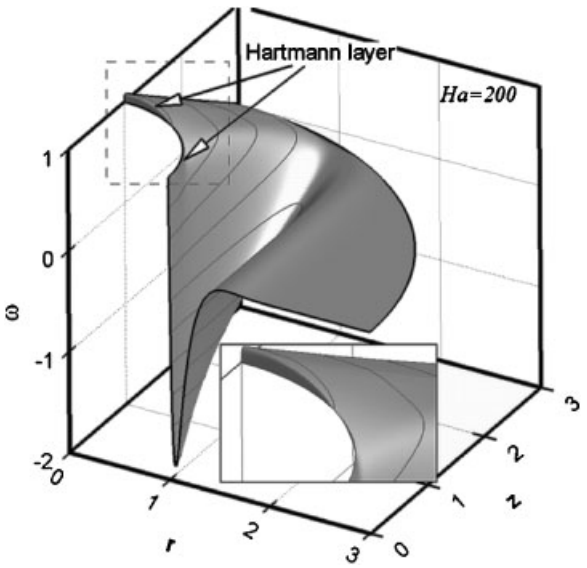

Figure 11. Distribution of angular velocity of circumferential flow $\omega(r, z)$ for a rotating sphere (case B). Enlarged view shows the Hartmann layers at the inner sphere.

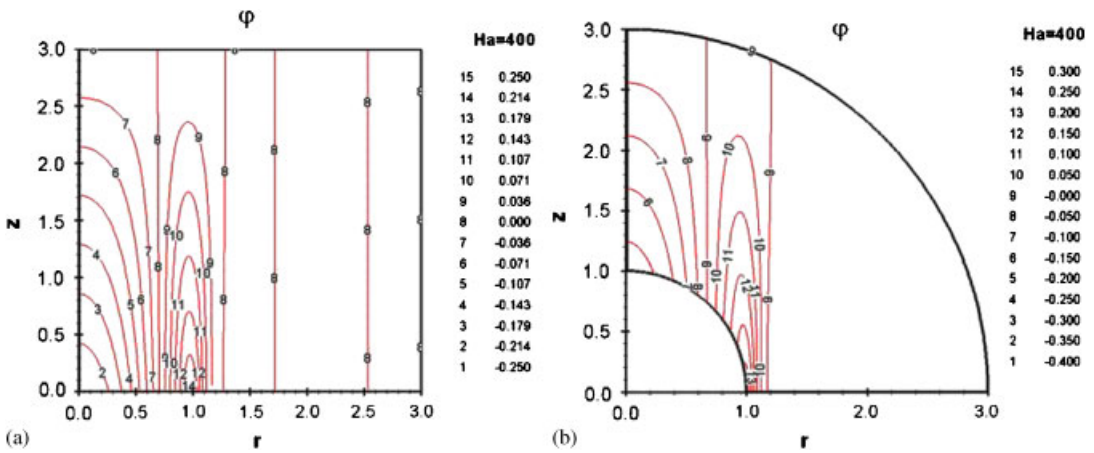

Figure 12. Electric potential fields for the cylindrical (a) and the spherical (b) shells.

The distribution of electric potential in the inner core remains approximately the same for all values of *Ha* studied (see Figure 12). The local value of the potential at the edge ($r = 1$) determines the magnitude of the jet at the symmetry plane. It should be noted that the local potential gradients appearing at the edge of the rotating disk become steeper as *Ha* increases. This is caused by the fact that the potentials in both cores approach final values as *Ha* increases while the thickness of the layer decreases. As shown in Figure 12(a) the pattern of electric potential is divided into an inner and an outer core. The inner core ($r < 1$) is due to the imposed boundary condition on the

DOI: 10.1002/fld

rotating disk with a linear variation of the potential along the z-axis. The outer core potential is preserving the boundary value ($\varphi=0$) imposed by the perfectly conducting walls. For $Ha\gg 1$ the electric potential approaches the relation

$$\varphi(r,z)=\left(\frac{1}{2}r^2+C\right)\left(\frac{Z-z}{Z}\right) \tag{29}$$

where r and z are the radial and axial coordinates and in this case the function Z is simply a constant, namely $Z(r)=3$, the total width of the fluid domain measured from the symmetry plane along the magnetic field lines at radial position r. The maximum value of the electric potential tends to reach the value $\phi(r=1,z=0)=0.25$ at the edge of the rotating disk as $Ha\to\infty$, in accordance with the asymptotic theory. Viscous effects in the parallel layer determine its width at $r=1$, i.e. the thickness of the layer depends on the Hartmann number.

All the preceding observations about the electric potential for the case of the rotating disk are valid also for the rotating sphere. The potential along the rotating sphere is proportional to r^2 and decays, for strong magnetic fields, linearly along z to zero at the outer wall. For $Ha\gg 1$, the potential in the inner core approaches the distribution

$$\varphi(r,z)=\left(\frac{1}{2}r^2+C\right)\left(\frac{Z-z}{Z-Z_\mathrm{b}}\right) \tag{30}$$

where now $Z(r)=\sqrt{R^2-r^2}$ and $Z_\mathrm{b}(r)=\sqrt{R_\mathrm{b}^2-r^2}$ denote the total extension of flow domain measured along the magnetic field lines at position r, the quantities R and R_b being the radii of the outer and inner shells, respectively. The value of C differs from that of the rotating disk case, and numerical simulations performed for $R=3$ confirm the trend that the highest potential values in the horizontal symmetry plane approach those obtained earlier by asymptotic theory $\varphi(1,0)\to 0.2613$ as $Ha\to\infty$.

The influence of fluid inertia introduced by centrifugal forces for finite Reynolds numbers leads to a meridional motion in the r–z plane as already shown in Figures 5 and 6. The strongest meridional motion is observed for the hydrodynamic case ($Ha=0$), which is progressively damped with increasing magnetic field. The kinetic energy of the meridional motion defined here as

$$E=\int_0^R\int_{Z_b(r)}^{Z(r)}(V_\mathrm{r}^2+V_z^2)2\pi r\,\mathrm{d}z\,\mathrm{d}r \tag{31}$$

is used as a measure to quantify the intensity of magnetic damping.

For the present flows, E depends on the Reynolds and Hartmann numbers, and in the absence of a magnetic field exclusively on Re. For the hydrodynamic flow, with fixed Reynolds number $Re=1$, the kinetic energy of the meridional motion is $E_0=2.81\times 10^{-4}$ for case A, and $E_0=1.46\times 10^{-4}$ for case B. These values are used to normalize the MHD results shown in Figure 13. When the formation of the two cores and the parallel layer has been established, the meridional motion is weakened significantly. Consequently, the kinetic energy of the meridional motion is considerably lower compared with the one of the pure hydrodynamic case.

Figure 13 shows the influence of the magnetic field on the intensity of the meridional fluid motion for both cases studied. It is interesting to note that the kinetic energy of the meridional motion for the rotating disk decays like Ha^{-3} for strong magnetic fields ($Ha>20$) while for the case of the rotating sphere it decays like Ha^{-2}. Even before Ha reaches 100, the meridional motion has already lost roughly four orders of magnitude of its kinetic energy. This result confirms that

DOI: 10.1002/fld

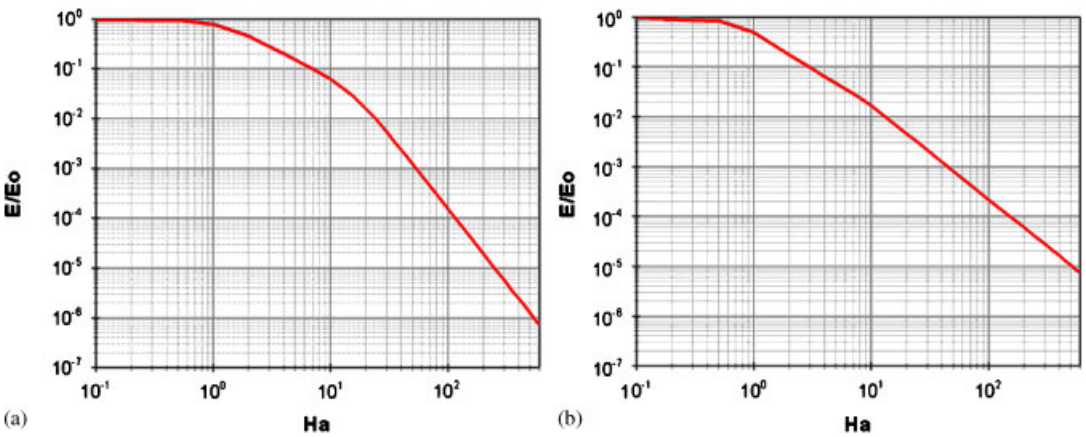

Figure 13. Variation of kinetic energy E of meridional motion with Ha (normalized by E_0 of the hydrodynamic flow) for the cylindrical (a) and the spherical (b) shells.

the meridional fluid motion (driven by inertia) is clearly negligible at high Ha and it is important since meridional motions have been disregarded in asymptotic methods. However, for low Ha, the meridional motion affects the development of the jet and the core flow in a way that cannot be described fully by analytic methods.

The raising of Ha reduces the width and increases the maximum velocity of the counter-rotating shear layers. The reversed jet in the tangent layer establishes a balance between viscous and electromagnetic forces. It is known that, for $Ha \gg 1$, the velocity and thickness of parallel layers, in which such regimes are present, scale like $u \sim Ha^{1/2}$ and $\delta \sim Ha^{-1/2}$. This asymptotic behaviour is confirmed by the results for the angular velocity of circumferential flow, which scale by $Ha^{1/2}$ as a function of the stretched radial coordinate:

$$x = (r-1) \cdot Ha^{1/2} \tag{32}$$

Figure 14 shows scaled velocity profiles in the tangential layer with respect to the stretched layer-normal coordinate. With increasing Ha, the profiles of circumferential velocity coalesce to a similar graphical representation. Indeed, the lines corresponding to high Ha cases have almost identical shape, giving a sense of asymptotic behaviour.

Figure 15 shows the maximum magnitude of the angular velocity of circumferential flow in the tangential layer. For low or moderate Hartmann numbers, the velocities differ and in fact are smaller than the asymptotic predictions. This is not surprising, since the asymptotic theory does not apply for such small Ha values. The influence of viscosity is strong enough to reduce the maximum velocity in the layer for smaller Ha. This is taken properly into account by the present numerical model, which solves the full transport equations including viscous and inertial terms. For higher Ha, the numerical values of $\omega_{\max}$ increase and converge monotonically towards the asymptotic solutions. It is found that for both cases (disk and sphere) the maximum angular velocity of circumferential flow scales as $\omega_{\max} \sim Ha^{1/2}$ for $Ha \gg 1$, in agreement with the asymptotic theory.

The results for the sphere follow the asymptotic solution precisely (even better than those of the disk) for high Hartmann numbers and they are in very good agreement with the analytical

DOI: 10.1002/fld

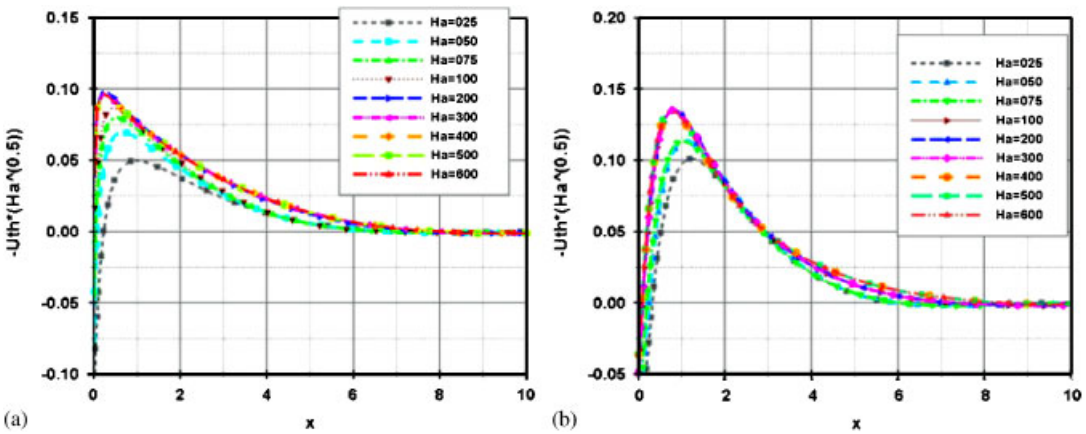

Figure 14. Variation of normalized circumferential jet velocity $(-V_\theta/\sqrt{Ha})$ with respect to the stretched layer-normal coordinate $x=(r-1)\sqrt{Ha}$.

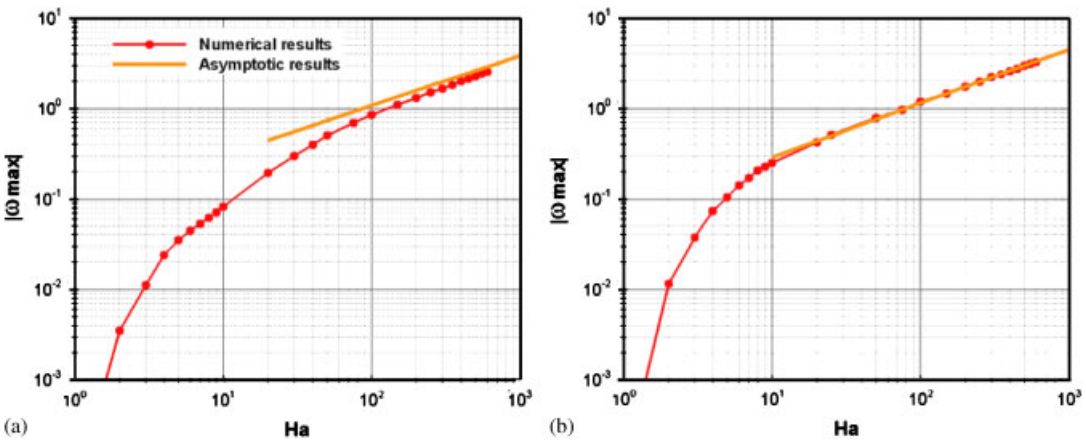

Figure 15. Comparison of numerical and asymptotic results of $\omega_{\max}$ in the parallel layer at various Ha, for the cylindrical (a) and the spherical (b) shells.

predictions of Bühler [1]. A reason for this good agreement is the curvature of the inner spherical boundary. The non-orthogonal inclination of the boundary with respect to the magnetic field leads to a thickening of the Hartmann layers that are now easier to resolve numerically near $r=1$. Moreover, the global behaviour seems to be less 'singular' in the sense that the numerical solutions verify that, for the sphere

$$\partial_z \varphi_{\text{sphere}}(z=0^+)=\partial_z \varphi_{\text{sphere}}(z=0^-)=\partial_z \varphi(z=0)=0 \quad \text{at } r=1 \tag{33}$$

while for the disk

$$\partial_z \varphi_{\text{disk}}(z=0^+)\neq\partial_z \varphi_{\text{disk}}(z=0^-)\neq\partial_z \varphi=0 \quad \text{at } r=1 \tag{34}$$

DOI: 10.1002/fld

where φ_{sphere} and φ_{disk} stand for the fluid potential at the sphere and the disk, respectively. This leads finally to a better performance of the numerical model for the case of the rotating sphere which yields smooth solutions near $r=1$. The case of the rotating disk, however, shows a singular behaviour for $\partial_z \varphi$ at the edge of the disk, which increases the computational difficulties for this type of flows.

From an engineering point of view it is interesting to know the torque that is necessary to rotate the disk or the sphere at a desired speed. Since the rotating disk is electrically conducting, it is necessary to overcome the braking torque created by viscous stresses at the surface of the rotating body plus the electromagnetic torque due to the circumferential Lorentz forces on the conducting body. Details for the derivation of the expressions for the torques are presented in the Appendix.

The viscous part of the torque is obtained by integration of the viscous stress over the surface of the rotating body

$$T_{\text{v}} = \frac{2\pi}{Ha^2} \int_S \partial_n V_\theta r^2 \, \mathrm{d}s \tag{35}$$

where ds is a line element along the contour of the rotating body.

The total radial current that creates the braking Lorentz torque on the body is calculated from the balance of the current density entering and leaving the body, yielding the total electromagnetic torque:

$$T_{\text{EM}} = \int_0^1 I(r) r \, \mathrm{d}r = -2\pi \int_0^1 \left(\int_0^r \partial_z \varphi r' \, \mathrm{d}r' \right) r \, \mathrm{d}r \tag{36}$$

Figure 16 shows the evolution of the electromagnetic torque T_{EM} and the ratio of electromagnetic to viscous torque $T_{\text{EM}}/T_{\text{v}}$ for the cylindrical (case A) and spherical (case B) shells at different values of Ha. For high Hartmann numbers, the electromagnetic torque on the disk approaches

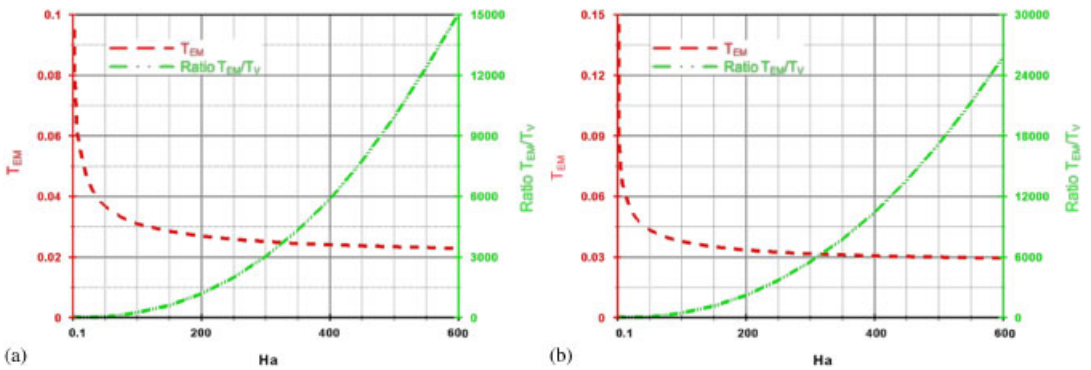

Figure 16. Variation of electromagnetic torque and ratio of electromagnetic to hydrodynamic torque with Ha for the disk (a) and the sphere (b).

DOI: 10.1002/fld

the constant value: $T_{\mathrm{EM}} \to -\pi/48Z = -0.0218$ for the present calculations with $Z = 3$, while the viscous torque is negligible in comparison with the electromagnetic one.

5. CONCLUSIONS

A numerical study of MHD flows in rotating cylindrical and spherical shells was performed with the aim to enhance the existing knowledge and to assess basic assumptions for treating these flows by asymptotic techniques. The present CFD model uncovered the main flow features previously observed.

For high Hartmann numbers, the results exhibit two different types of flow cores, one inside the tangent cylinder parallel to the magnetic lines, and the other outside it. The cores are separated by a thin, viscous tangential layer in which the fluid reaches the highest circumferential velocities. The inner core follows a solid-body rotation with the fluid near the perfectly conducting body rotating at the same angular velocity, which decays linearly in the axial direction. The outer core instead is practically stagnant.

In the case of the rotating disk, the Hartmann layers are absent since the obtained core solution satisfies already the no-slip boundary conditions at the disk and the outer walls. For the rotating sphere, instead, the inner core rotates faster than the sphere near the axis and slower close to the tangent cylinder. This is caused by the curvature of the inner and the outer boundaries and by the Hartmann length, i.e. the height of the gap measured along magnetic lines. As a result, there appear Hartmann layers at the rotating sphere, across which the no-slip condition is satisfied.

The properties of the counter-rotating jet that forms at the tangent cylinder parallel to magnetic lines at the edge of the rotating body were investigated in detail. The effect of the magnetic field on the velocity and thickness of the jet and the intensity of the meridional fluid motion were also assessed. The raising of Ha reduces the thickness of the tangential layer as $\delta \sim Ha^{-1/2}$ and increases its counter-rotation like $\omega \sim Ha^{1/2}$. The kinetic energy of the meridional motion driven by centrifugal forces is reduced proportional to Ha^{-3} for the disk and Ha^{-2} for the sphere, and it is already negligible at $Ha > 20$ compared with the hydrodynamic case.

The electric potential develops strong gradients in the transitional 'column' at the tangent cylinder. Its distribution in the inner core follows a linear decay in the axial direction and vanishes at the outer boundary. The driving mechanism of the rotating flow is the radial gradient of the potential that is observed in the inner core. However, the highest potential gradient (of opposite sign to that in the core) is observed in the symmetry plane at the perimeter of the rotating body, causing the highest counter-rotating velocities.

For the higher Ha values studied, all calculated quantities in the cores are in good agreement with asymptotic theory. The results obtained in the tangential layer differ slightly from those derived by analytic methods for the case of the rotating disk but they confirm the asymptotic behaviour. Very good agreement is achieved for the rotating sphere for which a proper numerical resolution of the Hartmann layer could be achieved easier, since this layer is not as thin as for the disk. Although the Hartmann layers do not carry a significant amount of electric current in these flows, their proper numerical resolution appears to be the key for accurate simulations.

The present work complements the known results, especially for perfectly conducting walls, and supports the asymptotic theory, usually applied for high Ha where meridional fluid motions are

DOI: 10.1002/fld

neglected *a priori*. For lower *Ha*, however, where the asymptotic theory is not valid, the present numerical model yields more reliable results.

APPENDIX A

Viscous torque: The differential viscous torque of a surface element $\mathrm{d}A = 2\pi r\,\mathrm{d}s$ at a distance r from the axis is given by the product:

$$\mathrm{d}T_{\mathrm{V}} = r\,\mathrm{d}F \tag{A1}$$

where $\mathrm{d}F = \tau\,\mathrm{d}A$ is the differential circumferential viscous force due to the shear stress

$$\tau = \frac{1}{Ha^2}\partial_n V_\theta \tag{A2}$$

The integration of (A1) along the contour of the rotating body yields the viscous part of the torque (for the sphere and disk) as

$$T_{\mathrm{v}} = \frac{2\pi}{Ha^2}\int_S \partial_n V_\theta r^2\,\mathrm{d}s \tag{A3}$$

where $\mathrm{d}s$ is a line element along the contour of the rotating body.

Electromagnetic torque: The total radial current that creates the braking Lorentz force on the body is calculated from the balance of the current density entering and leaving the body. The integration of this quantity along the contour of the body determines the total current $I(r)$ that flows radially in the revolving body

$$I(r) = \int_0^S j_n 2\pi r\,\mathrm{d}s = \int_0^r j_z 2\pi r\,\mathrm{d}r = -2\pi\int_0^r \partial_z \varphi r\,\mathrm{d}r \tag{A4}$$

creating at position r the elemental circumferential Lorentz force

$$\mathrm{d}F = I(r)\,\mathrm{d}r \tag{A5}$$

Integration of the differential electromagnetic torque

$$\mathrm{d}T_{\mathrm{EM}} = r\,I(r)\,\mathrm{d}r \tag{A6}$$

yields the total electromagnetic torque as

$$T_{\mathrm{EM}} = \int_0^1 I(r) r\,\mathrm{d}r = -2\pi\int_0^1 \left(\int_0^r \partial_z \phi r'\,\mathrm{d}r'\right) r\,\mathrm{d}r \tag{A7}$$

In the case of the rotating disk where $\mathrm{d}s = \mathrm{d}r$ and $\partial_n = \partial_z$, the torques may be calculated for high *Ha*. Then, the azimuthal velocity V_θ and the potential φ may be represented by

$$V_\theta = \left(1 - \frac{z}{Z}\right) r \tag{A8}$$

and

$$\varphi = \left(1 - \frac{z}{Z}\right)\left(\frac{1}{2}r^2 - \frac{1}{4}\right) \tag{A9}$$

DOI: 10.1002/fld

It follows that the torques asymptotically are given by

$$T_{\mathrm{V}} = -\frac{1}{Ha^2}\frac{2\pi}{Z} \tag{A10}$$

and

$$T_{\mathrm{EM}} = -\frac{\pi}{48Z} \tag{A11}$$

and, for $Z = 3$, the electromagnetic torque on the disk approaches the constant value: $T_{\mathrm{EM}} \to -0.0218$, a result that has been verified numerically.

Similar analytic calculations are not possible for the case of the rotating sphere because of the existence of the additional Hartmann layer above the sphere.

NOMENCLATURE

a_i	link coefficient in discretized equations
A	surface area
$\mathbf{B}$	magnetic induction vector
B_{o}	magnitude of magnetic field
C	constant
e	convergence criterion
E	kinetic energy of meridional motion
F	force
Ha	Hartmann number
I	current
$\mathbf{j}$	current density vector
L	reference length
N	interaction parameter
p	pressure
r	radius
$\mathbf{r}$	unit vector in radial direction
R	radius of outer shell
Re	Reynolds number
r_{o}	radius of rotating body
S_i	source term
T	torque
T_{EM}	electrodynamic torque
T_{V}	hydrodynamic torque
u_{o}	velocity reference quantity
$\mathbf{v}$	velocity vector
V	cell volume
V_{r}	radial velocity
V_z	axial velocity
V_θ	Azimuthal/Circumferential velocity
Z	total domain height

DOI: 10.1002/fld

$\mathbf{z}$	unit vector in the axial direction
z_b	contour of the rotating body

Greek letters

δ	tangential layer thickness
δ_r	radial length cell increment
δ_z	axial length cell increment
$\boldsymbol{\theta}$	unit vector in the azimuthal direction
ν	fluid kinematic viscosity
π	Archimedes' constant
ρ	fluid density
σ	electric conductivity
τ	shear stress
φ	electric potential
ω	angular velocity of circumferential flow

Subscripts

b	boundary line
n	normal component
nb	neighbouring cells
p	current cell
r	radial component
θ	azimouthal/circumferential component

Superscripts

$*$	initial guessed value
$'$	correction value

ACKNOWLEDGEMENTS

This work was performed under the Euratom–Hellenic Republic and Euratom–FZK Association agreements. The research is supported by the Euratom Fusion Programme and the General Secretariat for Research & Technology (GSRT) of Greece. The leading author (DF) benefited from a doctoral research grant by the Greek Fusion Programme. The content of this publication is the sole responsibility of its authors and it does not necessarily represent the views of the European Commission, the GSRT or their Services.

REFERENCES

1. Bühler L. On origin of super-rotating tangential layers in magnetohydrodynamic flows. Forschungszentrum Karlsruhe Gmb, *FZKA 7028*, 2004.
2. Antimirov MY, Molokov SY. Magnetohydrodynamic flow in the rotation of a disk in a strong magnetic field. *Magnetohydrodynamics* 1989; **25**:71–76.
3. Hollerbach R, Skinner S. Instabilities of magnetically induced shear layers and jets. *Proceedings of the Royal Society London*, *Series A* 2001; **457**:785–802.

DOI: 10.1002/fld

4. Bessaih R, Marty P, Kadja M. Numerical study of disk driven rotating MHD flow of a liquid metal in a cylindrical enclosure. *Acta Mechanica* 1999; **135**:153–167.
5. Kharicha A, Alemany A, Bornas D. Influence of the magnetic field and the conductance ratio on the mass transfer rotating lid driven flow. *International Journal of Heat and Mass Transfer* 2004; **47**:1997–2014.
6. Molokov SY. Single-component Magnetohydrodynamic flows in a strong uniform magnetic field. 2. Rotation of an axisymmetric body. *Magnetohydrodynamics* 1993; **29**:81–86.
7. Dormy E, Jault D, Soward AM. A super-rotating shear layer in magnetohydrodynamic spherical Couette flow. *Journal of Fluid Mechanics* 2002; **452**:263–291.
8. Starchenko SV. Magnetohydrodynamic flow between insulating shells rotating in strong potential field. *Physics of Fluids* 1998; **10**:2412–2420.
9. Hunt JCR, Malcolm DG. Some electrically driven flows in magnetohydrodynamics. Part 2. Theory and experiment. *Journal of Fluid Mechanics* 1968; **33**:775–801.
10. Müller U, Bühler L. *Magnetofluiddynamics in Channels and Containers*. Springer: Wien, New York, 2001. ISBN-10:3540412530.
11. Ferziger JH, Peric M. *Computational Methods for Fluid Dynamics* (3rd rev. edn). Springer: Berlin, 2002. ISBN-10:3540420746.
12. Baxevanou CA, Vlachos NS. A comparative study of numerical schemes and turbulence models for wind turbine aerodynamic modelling. *Wind Engineering* 2004; **28**:275–290.
13. Fidaros D. Numerical Simulation and Study of MHD Flows in Curvilinear Geometries. *Internal Report*, *FMTL-UTH*, *2005*, *PhD Thesis*, University of Thessaly, 2007.
14. Cho MJ. Discretization of Lorentz force term. *Numerical Heat Transfer*, *Part B*: *Fundamentals* 2006; **49**:599–615.
15. Van Doormaal JP, Raithby GD. Enhancements of the SIMPLE method for predicting incompressible fluid flows. *Numerical Heat Transfer* 1984; **7**:147–163.
16. Versteeg HK, Malalasekera W. *An Introduction to Computational Fluid Dynamics. The Finite Volume Method*. Logman: New York, 1995. ISBN-10: 0582218845.
17. Shewchuk JR. An introduction to the conjugate gradient method without the agonizing pain. *Technical Report CMUCS-94-125*, Carnegie Mellon University, 1994.
18. Drikakis D, Rider W. *High-Resolution Methods for Incompressible and Low Speed Flows*. Springer: Berlin, 2005. ISBN: 3-540-22136-0.
19. Ni M-J, Munipalli R, Morley NB, Huang P, Abdou MA. A current density conservative scheme for incompressible MHD flows at a low magnetic Reynolds number. Part I: On a rectangular collocated grid system. *Journal of Computational Physics* 2007; **227**(19):174–204.

DOI: 10.1002/fld